Check for updates

ZnS quantum dots impregnated-mesoporous TiO₂ nanospheres for enhanced visible light induced photocatalytic application†

S. Harish,[a] M. Sabarinathan,[a] A. Periyanayaga Kristy,[b] J. Archana,[b] M. Navaneethan, [ID] *[a] H. Ikeda[a] and Y. Hayakawa [ID] *[a]

ZnS quantum dots were impregnated on the surface of TiO₂ mesospheres by a soft template-assisted solvothermal approach. XRD and elemental analysis confirmed the presence of ZnS in the TiO₂ nanostructures. Morphological analysis showed that the ZnS quantum dots were firmly immobilized on the TiO₂ mesospheres, which improved electron and hole pair separation at the TiO₂/ZnS interface. The photocatalytic activity of the mesoporous nanostructures was assessed by photodegradation of methylene blue (MB) as a model pollutant under visible light irradiation. Impregnation with ZnS quantum dots enhanced reaction activity remarkably compared with mesoporous TiO₂. The maximum degradation efficiency was observed for 0.025 M of ZnS impregnated on TiO₂. The MB-related absorption peak completely disappeared after 32 min of irradiation. Photo-charge scavenger analysis indicated that hydroxyl radicals played a pivotal role in the photodegradation mechanism. The mesoporous photocatalyst was stable and can be used repeatedly under visible irradiation.

Introduction

Removal of hazardous inorganic heavy metal pollutants is vital in water purification.[1–3] The search continues for an economic and efficient method to remove such pollutants from wastewater and reduce negative environmental impacts. Heterogeneous photocatalysis is a popular technique with great potential in degradation of organic pollutants, and has proven to be effective in environmental remediation.[4] A photocatalysis semiconductor can be used to generate electron–hole pairs by absorbing light with photonic energy, which simultaneously initiates oxidation and reduction with surface species before recombination.[5–7] The organic compounds are decomposed into the less toxic materials CO_2 and water.[2,8] TiO₂ is one of the best photocatalysts for the self-cleaning environmental applications because of its relatively high efficiency, low cost and its availability. TiO₂ has been widely used as a photocatalyst for removal of hazardous organic substances and as an electrode material for dye-sensitized solar cells[9,10] because of its strong oxidizing and reducing ability under UV light irradiation.

Mesoporous TiO₂ is an interesting structure for photocatalytic applications because of its continuous particle framework, which is beneficial for catalyst recovery when compared with nanoparticles.[11] The photocatalytic activity of mesoporous TiO₂ is affected by larger surface area that increases the reaction rate, while the existence of amorphous phases promotes e− and h+ recombination, which in turn decreases photocatalytic activity. Additionally, in the photocatalytic field, the pores of nanostructures can serve as channels for charge carriers to penetrate the interior and reduce the recombination rate, thus enhancing the activity.[12] To exploit its excellent photocatalytic performance, much effort has been devoted to synthesis of mesoporous TiO₂ in recent years. Attempts have been made to control the crystallization and to make more crystalline material with maintenance of mesoscale order.[13] Da Silva *et al.*[14] prepared truncated bipyramidal Wulff-shape mesoporous TiO₂ by nonaqueous sol–gel synthesis, and this exhibited superior photocatalytic activity. Liu *et al.*[15] synthesized spindle-shaped mesoporous TiO₂ using an aqueous peroxotitanium solution with polyacrylamide. However, in recent years, development of visible light active photocatalysts has received major attention because of potential applications for indoor self-cleaning and self-sterilizing surfaces such as glass and ceramic tiles.[16–18] Several strategies have been adopted for preparation of such visible light active photocatalysts. Metal doping of mesoporous TiO₂ structures is thought to be a good way to enhance the photocatalytic activity, while the coupling of TiO₂ with another semiconductor is another widely used approach.[19–24] Semiconducting metal sulphides have light absorbing ability in the visible and near-infrared region, which makes them

[a] Research Institute of Electronics, Shizuoka University, 3-5-1 Johoku, Naka-ku, Hamamatsu, Shizuoka 432-8011, Japan. E-mail: mpnavaneethan@yahoo.co.in; royhaya@ipc.shizuoka.ac.jp; Fax: +81 53 4781338; Tel: +81 53 4781338

[b] SRM Research Institute, Department of Physics and Nanotechnology, SRM University, Kattankulathur, Chennai, 603203, Tamil Nadu, India

† Electronic supplementary information (ESI) available. See DOI: 10.1039/c7ra03061d

promising as visible-light driven photocatalysts.[25–29] In particular, ZnS has been studied in many applications as it is an environmentally friendly material and is constituted by earth-abundant elements.[30] ZnS is an important II–VI semiconductor exhibiting a wide direct optical band gap (3.6 eV), making it a very attractive material for optical applications, especially in its nanocrystalline form. Photocatalytically active TiO_2/ZnS composites show better photostability and activity than do their individual components. Vaclav *et al.*[31] synthesized a TiO_2/ZnS nanocomposite by homogeneous hydrolysis in an aqueous solution of thioacetamide. The prepared composite showed better photocatalytic activity compared with bare TiO_2 and ZnS nanoparticles. Xiaodan *et al.*[32] prepared photoactive ZnS/TiO_2 nanocubes *via* a microemulsion-mediated solvothermal method. The photocatalytic activity of ZnS/TiO_2 composites was enhanced compared with pure anatase TiO_2 under visible light irradiation. Srinivasa Rao *et al.*[33] synthesized a TiO_2/ZnS photo-anode on fluorine-doped tin oxide (FTO), which accumulated a large number of photo-injected electrons in the conduction band (CB) and achieved lower recombination rate compared with bare TiO_2. Franco *et al.*[34] synthesized a distinct nanocrystalline TiO_2-capped ZnS using a chemical vapour deposition method. The TiO_2-capped ZnS increased the catalyst photoactivity compared with bare TiO_2. However, all these reports are related to the TiO_2 nanoparticles and ZnS – any interaction between the ZnS nanoparticles and TiO_2 nanoparticles is not discussed. Therefore, research is required into the ZnS included TiO_2 mesoporous network, with the aim of to extending charge separation and ultrafast degradation under visible light irradiation. To date, no research has been reported on mesoporous TiO_2/ZnS nanospheres.

The present study describes a soft template route to synthesize ZnS quantum dot impregnated mesoporous TiO_2 spheres with enhanced photocatalytic activity. The effect of metal sulphide concentration on the phase and morphology was investigated. The functional properties of mesoporous TiO_2 spheres were investigated using X-ray diffraction (XRD), field-emission scanning electron microscopy (FESEM), transmission electron microscopy (TEM) and X-ray photoelectron spectroscopy (XPS). The photocatalytic activity of the synthesized materials was characterized by quantifying the rate of methylene blue (MB) degradation in the aqueous suspension under visible light irradiation. The photostability and photocatalytic mechanism of mesoporous TiO_2 is proposed.

Experimental method

All chemicals were purchased from Wako Chemicals (Japan) and used without further purification. Three steps were followed for preparation of mesospheres TiO_2/ZnS mesoporous nanostructures.

Formation of titania glycolate spheres

1 mL of titanium tetraisopropoxide was added to 50 mL ethylene glycol. The solution was stirred at room temperature, and then added to an acetone bath (150 mL) containing trace water. The solution was stirred for 2 h to form a white suspension, which was collected by centrifugation, thoroughly washed with distilled water and ethanol to remove impurities, and dried at 100 °C for 10 h.

Formation of mesoporous TiO_2 spheres

The titania glycolate spheres were dispersed in an equal volume of water and ethanol (30 mL), and stirred for 2 h. The white solution was transferred to a 100 mL Teflon-lined stainless steel autoclave, and heated at 150 °C for 12 h. The resulting product was collected and annealed at 300 °C for 2 h.

Formation of mesoporous TiO_2/ZnS nanocomposites

The mesoporous TiO_2 spheres were dispersed in 50 mL of water and different mole concentrations of zinc acetate (0.025, 0.050, 0.075 and 0.1 M) and thioacetamide (0.025, 0.050, 0.075 and 0.1 M) were added. Pyridine was added as a capping ligand. The reaction was stirred for 12 h. The white solution was transferred to a 100 mL Teflon-lined stainless steel autoclave, and heated at 150 °C for 15 h. The resulting product was collected and dried at 100 °C for 10 h. The sample were termed as Ti for pure mesoporous TiO_2, TiZ-1 for 0.025 M of ZnS, TiZ-2 for 0.050 M of ZnS, TiZ-3 for 0.075 M of ZnS and TiZ-4 for 0.1 M of ZnS, respectively.

Characterization

Surface morphologies were observed using JEOL JSM 7001F field-emission scanning electron microscopy (FESEM). Transmission electron microscopy (TEM) images were recorded using a JEOL JEM 2100F microscope at an accelerating voltage of 200 kV. Crystalline phases were obtained by X-ray diffraction (XRD), using a Rigaku diffractometer (RINT-2200, Japan, CuK$_\alpha$ radiation) with a $0.02°$ s^{-1} scan rate. Raman spectra were obtained using a JASCO NR-1800 spectrometer. Ultraviolet-visible (UV-vis) absorption spectra were measured using a Shimadzu 3100 PC spectrophotometer (Japan). X-ray photoelectron spectroscopy (XPS) were recorded by a Shimadzu ESCA 3400.

Photocatalytic studies

The photocatalytic activity of the synthesized samples was evaluated at room temperature under a xenon light source (MAX-303, Asahi Spectra) as a source of visible-light irradiation. In a typical reaction, the dye concentration was fixed at 10 ppm and a known dosage (50 mg L^{-1}) of photocatalyst was added to the dye solution. The suspension was stirred to achieve an absorption–desorption equilibrium state of the solution, which was kept in the dark before light irradiation.[35,36] The reaction mixture was irradiated with stirring under the halogen lamp positioned at 21 cm above the reaction mixture. The reaction vessel consisted of an external jacket for water circulation to maintain the reaction mixture at room temperature. At regular time intervals, 3 mL of the suspension was collected, centrifuged, and analyzed using a UV-vis spectrometer. The MB degradation was estimated from the decrease in the intensity of the associated characteristic band absorption at 664 nm. The

Fig. 4 XPS spectra of O 1s state of mesoporous samples.

at binding energies of 458.46 eV (Ti $2p_{3/2}$) and 464.42 eV (Ti $2p_{1/2}$), which were assigned to Ti^{4+} in anatase titanium.[41,42] The separation between the Ti $2p_{3/2}$ and Ti $2p_{1/2}$ was 5.9 eV, consistent with the reported value of TiO_2.[43] The binding energies of sample TiZ-1 were shifted to 458.91 eV and 464.68 eV from 458.46 eV and 464.42 eV compared with mesoporous TiO_2. Furthermore, increasing the concentration of ZnS caused the peaks to shift to 459.14 eV and 464.73 eV for sample TiZ-2, 459.24 eV and 464.96 eV for sample TiZ-3 and 459.35 eV and 465.05 eV for sample TiZ-4. The binding energy of Ti 2p shifted to higher energy with increasing ZnS concentration.[44]

The Zn $2p_{3/2}$ and $2p_{1/2}$ peaks were located at 1022.57 and 1045.52 eV, respectively [Fig. 3(b)], illustrating formation of ZnS.[45] The difference between the two binding energies was 22.95 eV, which is in good agreement with the standard value of

22.97 eV.[46] The position of peaks in sample TiZ-4 shifted from 1022.57 eV to 1022.96 eV and from 1045.52 eV to 1046.05 eV compared with sample TiZ-1. As the ionic radius of Zn^{2+} is slightly larger 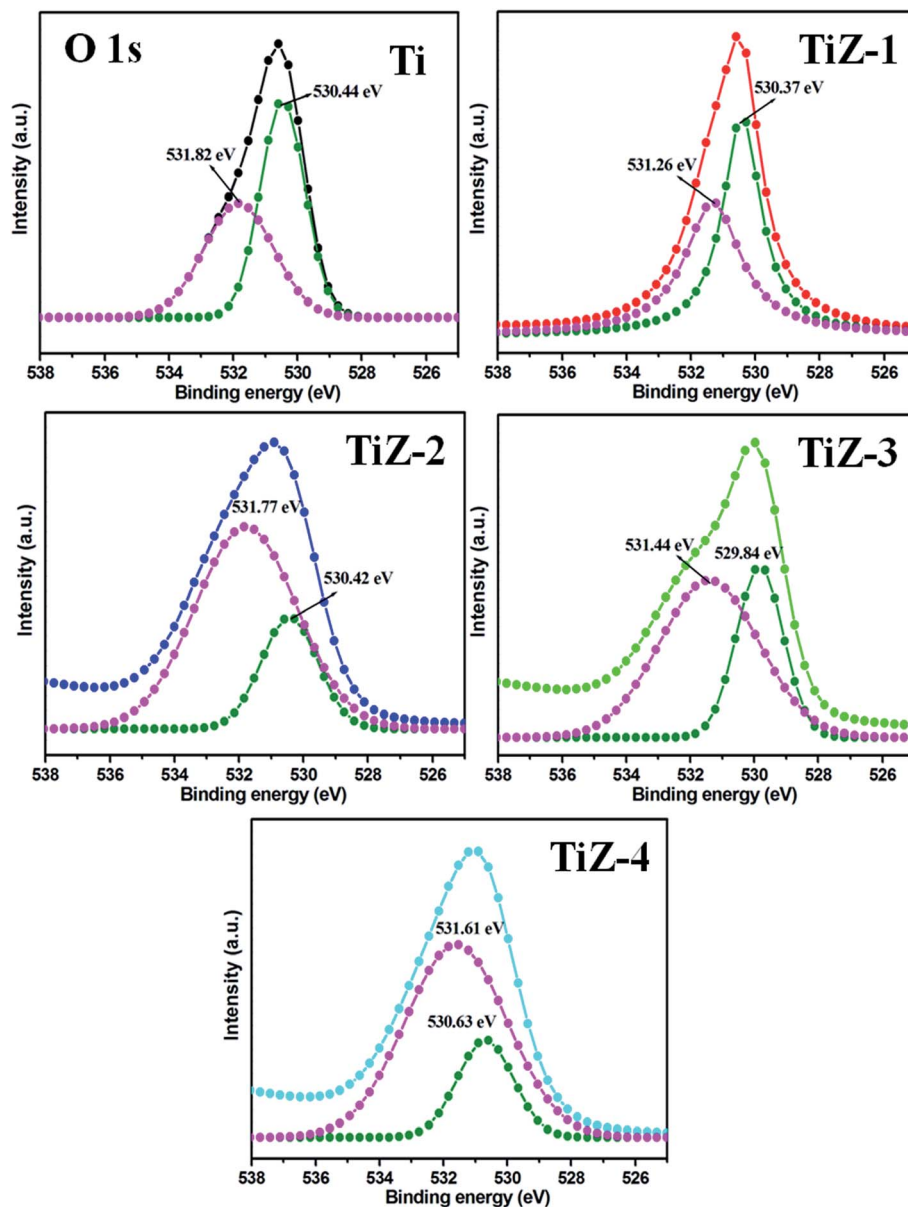than that of Ti^{4+}, substituting the Zn atom in the TiO_2 crystal structure could slightly distort the anatase crystal.[47,48] These observations indicated possible diffusion of Zn in mesoporous TiO_2. The peak at 225.81 eV corresponded to S 2s state [Fig. 3(c)], consistent with the reported value.[49] A similar shift of peak from 225.81 eV to 226.75 eV was observed with increasing Zn content. According to the high-resolution scan spectra, the binding energies of Ti 2p, Zn 2p, S 2s and O 1s shifted to higher values as the concentration of Zn increased in the composites, suggesting changes in the chemical environment. Binding energy was dependent on shielding effect caused by the electron density around atoms. Hence, the

increase in the binding energy of Ti 2p and Zn 2p could be attributed to the enhanced electron density around Ti and Zn atoms with strong interaction. The binding energies of O 1s of TiO_2 and TiO_2/ZnS mesoporous nanostructures are shown in Fig. 4. The peaks are deconvoluted into two peaks centred at 530.44 and 531.82 eV (Ti sample) by Gaussian fitting, which corresponded to the contributions from the surface adsorbed hydroxyl groups[50,51] and Ti–O,[52,53] respectively. The peaks of composite samples shifted to 530.37 and 531.26 eV for sample

TiZ-1, 530.42 and 531.77 eV for sample TiZ-2, 529.84 and 531.44 eV for sample TiZ-3 and 530.63 and 531.61 eV for sample TiZ-4. On the basis of the above analyses, it can be concluded that there was strong interaction between ZnS and TiO_2 in TiO_2/ZnS composites. The interaction significantly modified the original chemical states and electronic properties in the nanocomposite.

Fig. 5–9 show the FESEM, TEM and HRTEM images of mesoporous TiO_2 and TiO_2/ZnS quantum dots. Fig. 5(a) shows
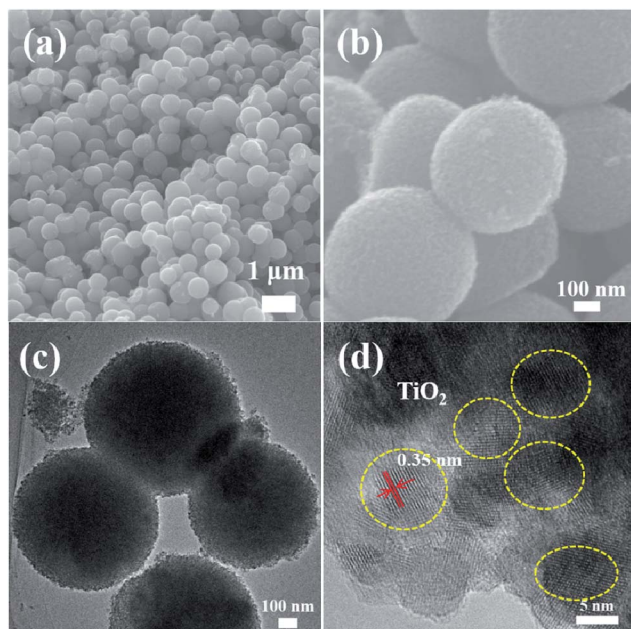
Fig. 5 (a) and (b) FESEM images of mesoporous TiO_2 spheres. (c) and (d) TEM and HRTEM images of mesoporous TiO_2 spheres.

Fig. 7 (a) and (b) FESEM images of mesoporous TiO_2/ZnS spheres. (c) and (d) TEM and HRTEM images of mesoporous sample TiZ-2.

Fig. 6 (a) and (b) FESEM images of mesoporous TiO_2/ZnS spheres. (c) and (d) TEM and HRTEM images of mesoporous sample TiZ-1.

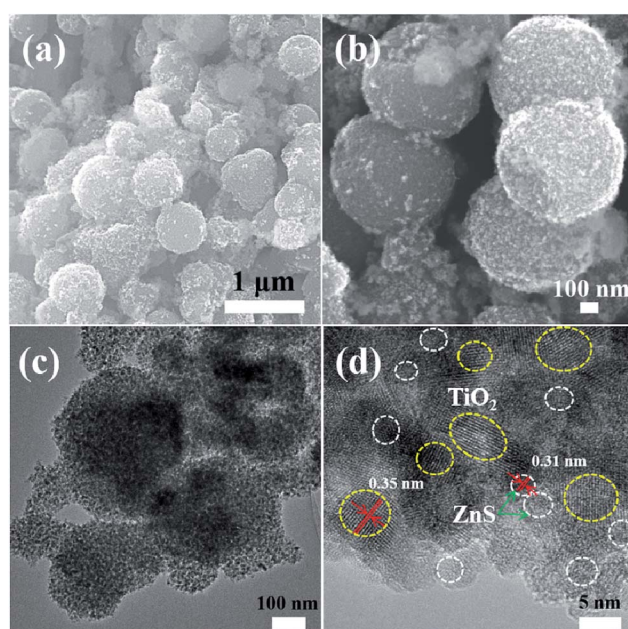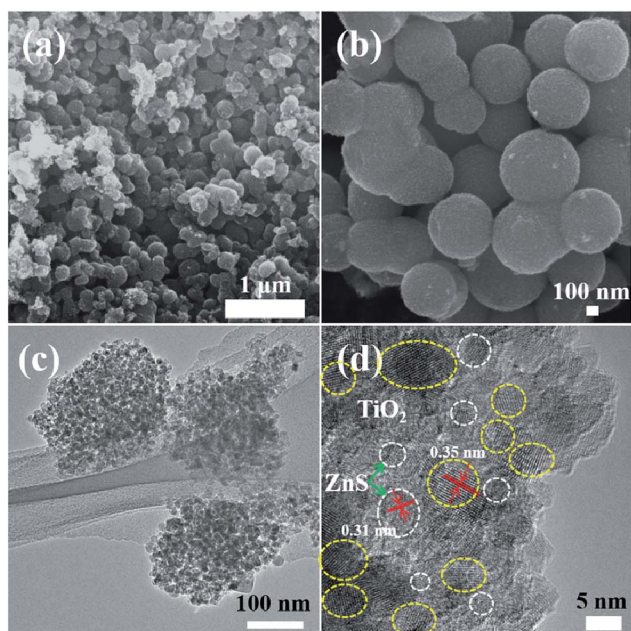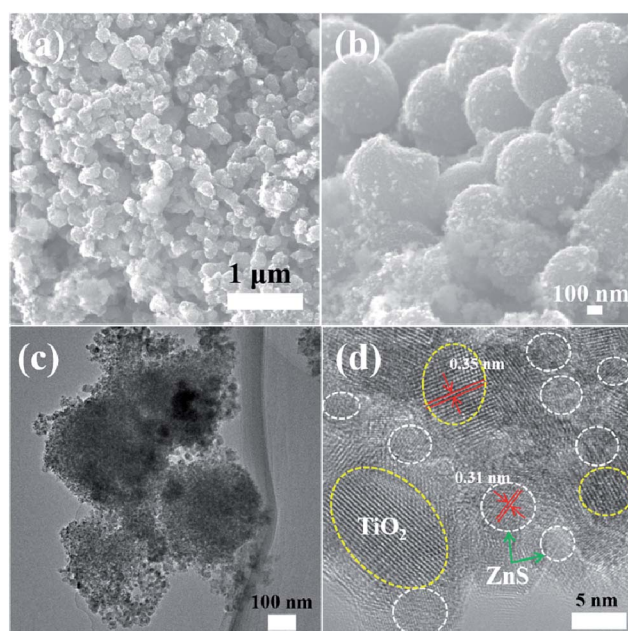**Fig. 8** (a) and (b) FESEM images of mesoporous TiO_2/ZnS spheres. (c) and (d) TEM and HRTEM images of mesoporous sample TiZ-3.

typical FESEM images of the titania glycolate spheres, which exhibited an average size of 400–500 nm with smooth surfaces. Porous TiO_2 spheres were formed after solvothermal treatment as shown in Fig. 5(b). A TEM image of the porous TiO_2 spheres is shown in Fig. 5(c). In addition, the presence of lattice fringes of mesoporous TiO_2 can be clearly observed in the HRTEM image, as shown in Fig. 5(d). Lattice fringe spacing is 0.35 nm and is in good agreement with the (101) lattice plane of anatase TiO_2. When the ZnS concentration was 0.025 M, ZnS quantum dot

was impregnated on the mesoporous TiO_2, as shown in Fig. 6(a). As the ZnS concentration increased to 0.050, 0.075 and 1.0 M, the morphology of the products became densely covered mesoporous TiO_2. The morphology of TiZ-1 was further analyzed by TEM, as shown in Fig. 6(c). The surface of the spheres was rough with surface decoration. At higher concentration, the surface of $TiO2$ was densely covered with ZnS nanoparticles. Fig. 6(d) displays the representative HRTEM image of the TiO2/ZnS mesospheres, with the white dashed line corresponding to ZnS quantum dots and the yellow dashed line corresponding to anatase TiO_2. The lattice fringe spacing of $TiO2$ (101) and ZnS (111) is 0.35 nm and 0.31 nm, respectively. The HRTEM images make evident that the TiO_2 nanocrystals are in close contact with the ZnS nanocrystals. The formation of a heterojunction (pink dashed line) enhanced transport of photogenerated electrons and holes between TiO_2 and ZnS. The ZnS nanoparticles were about 2–5 nm for TiZ-1, 2–6 nm for TiZ-2, 2–6 nm for TiZ-3 and 3–6 nm for TiZ-4, as shown in Fig. S1.† High resolution TEM images showed the good crystalline nature. Fig. 10 shows the elemental mapping of the Ti, Zn, O and S in the TiZ-1 sample. It is clearly evident that the Zn signal originated in a similar spatial area to that of the corresponding Ti signal. From the elemental mapping, it is confirmed that a composite distribution was formed in TiO_2/ZnS mesoporous nanostructure.

Fig. 9 (a) and (b) FESEM images of mesoporous TiO_2/ZnS spheres. (c) and (d) TEM and HRTEM images of mesoporous sample TiZ-4.

Photocatalysis

The photocatalytic activities of the mesoporous TiO_2 and TiO_2/ZnS quantum dots were evaluated by examination of MB dye degradation under visible light irradiation. The photocatalytic activities of prepared samples were tested by examining the degradation of organic pollutants (MB) as a function of time. The decrease in relative concentration of the MB was estimated
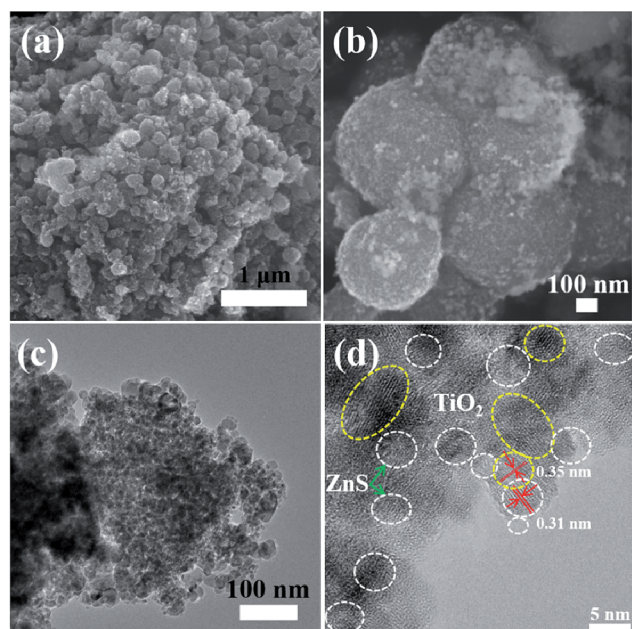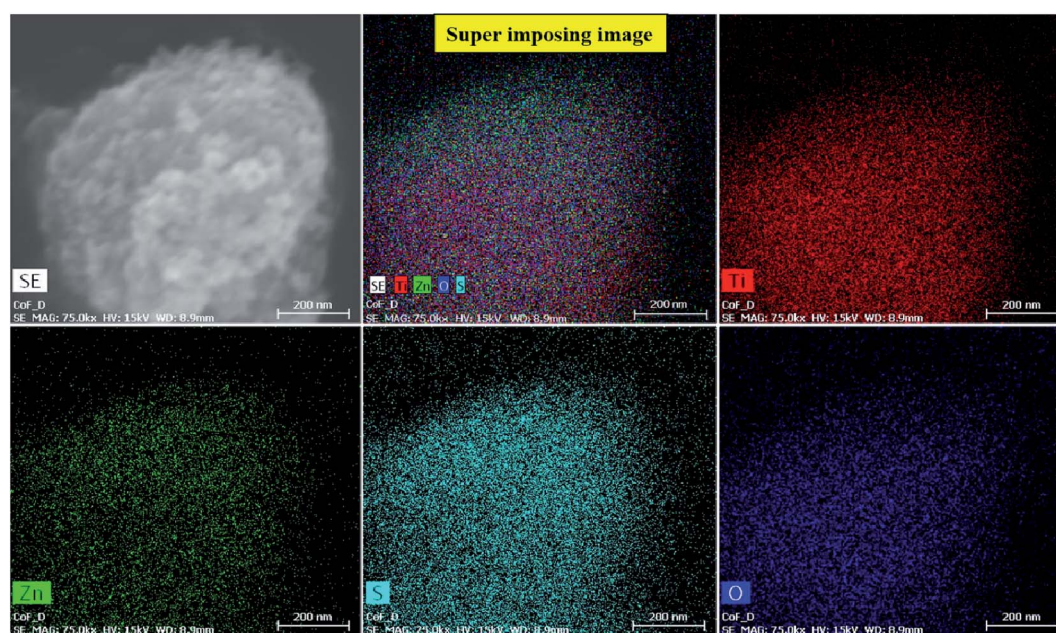
Fig. 10 Elemental mapping of sample TiZ-1.

by measuring the relative intensity of the peak at 664 nm from the optical absorbance spectra. Fig. 11(a) shows the time-dependent UV absorption spectra of mesoporous TiO$_2$ catalyst, which completely decomposed with irradiation time of 60 min. The effect of addition of different concentrations of TiO$_2$ as TiZ-1, TiZ-2, TiZ-3 and TiZ-4 is shown in Fig. 11(b–e).

Fig. 11(b) shows a rapid decrease in the initial absorbance of the peak, which disappeared completely after 32 min of irradiation. As the concentration of Zn was increased to 0.050, 0.075 and 0.1 M, photodegradation time increased to 40, 44 and 52 min, as shown in Fig. 11(c)–(e). Pure TiO$_2$ (Ti) exhibited the lowest photocatalytic activity, with TiO$_2$/ZnS composite showing
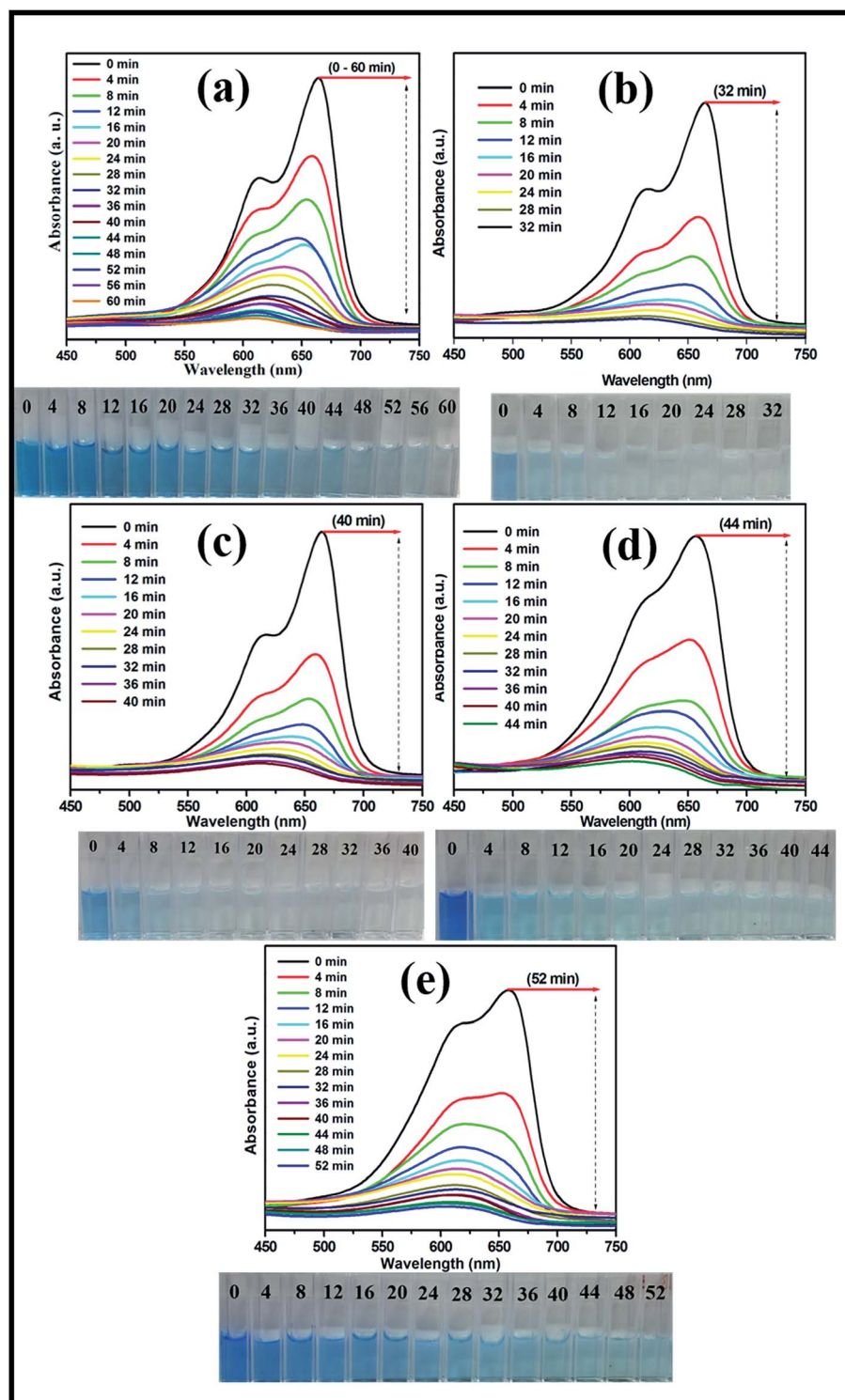
Fig. 11   UV absorption spectra of MB degradation of samples Ti, TiZ-1, TiZ-2, TiZ-3 and TiZ-4.

higher photocatalytic activity. Thus, it can be concluded that introduction of a very small amount of ZnS to the TiO$_2$ surface resulted in improved performance of dye degradation.

Fig. 12(a) shows the effect of mesoporous TiO$_2$ and TiO$_2$/ZnS nanocomposite on MB degradation. MB decolonization in the absence of catalyst was also evaluated. Less than 10% of the MB in the solution disappeared after 60 min of photolysis. The degradation rate of mesoporous TiO$_2$/ZnS catalysts decreased with increasing ZnS content from 0.025 M to 0.1 M. Sample TiZ-1 had the highest activity of all samples. As the photocatalytic

reaction is dependent on the surface atomic arrangement at the interface between the catalyst surface and organic pollutants,[54,55] the optimum content of ZnS is an important factor in the photocatalytic activity of the TiO$_2$/ZnS photocatalyst. Fig. 12(b) shows the schematic representation and pore size distribution of the mesoporous TiO$_2$ and TiO$_2$/ZnS photocatalyst. Addition of ZnS at different concentrations affected the structure of mesoporous TiO$_2$. At lower mole concentration (0.025 M and 0.050 M), the ZnS initiated growth of nanoparticles on the mesoporous TiO$_2$. Increasing the concentration
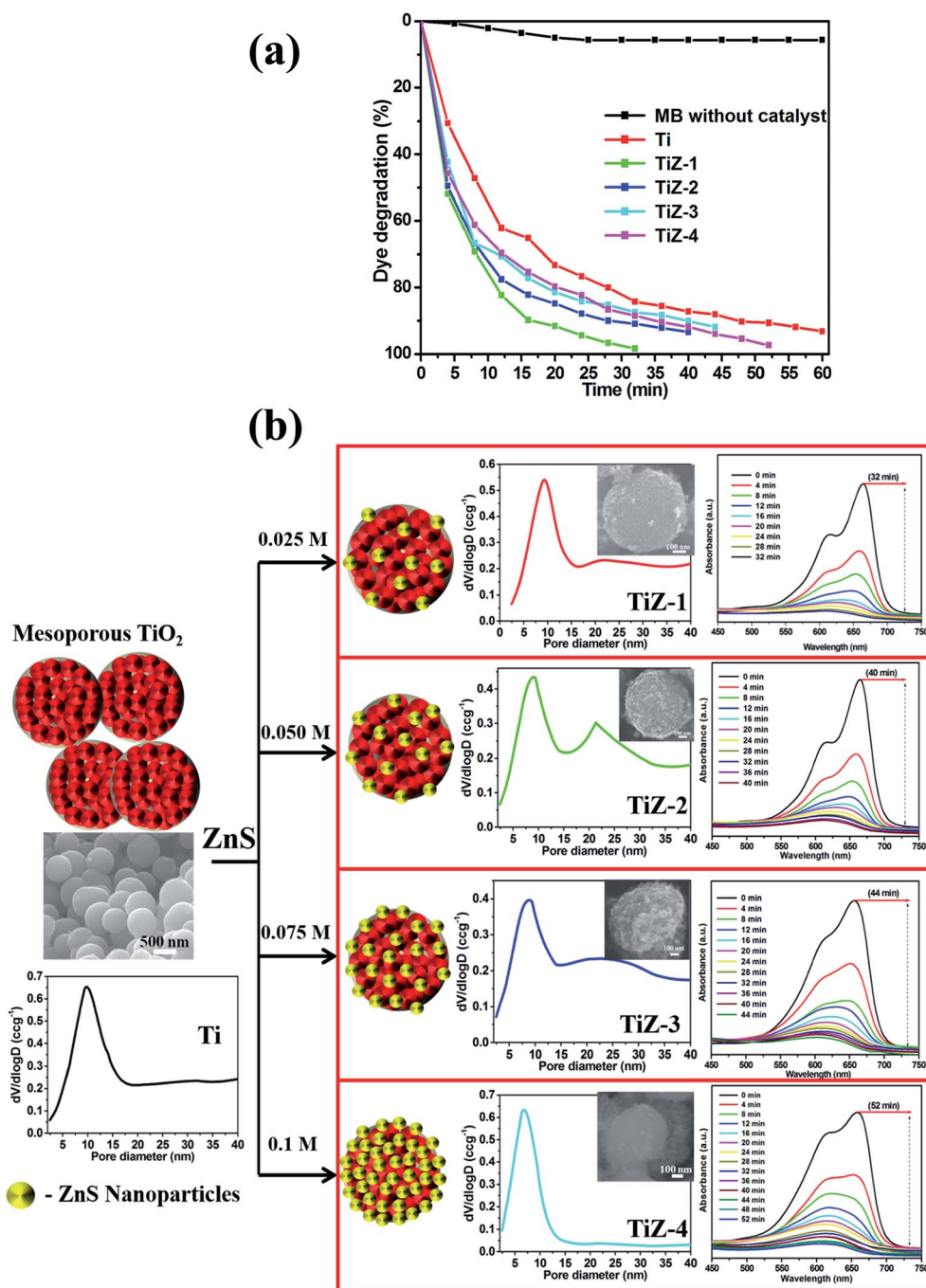

Fig. 12 Effect of dye degradation efficiency. (a) Time (min) *vs.* dye degradation (%) and (b) growth mechanism of TiO$_2$/ZnS mesoporous nanostructures.

of ZnS caused the number of ZnS nuclei to increase and the nanoparticles were grown completely on the mesoporous spheres. Thus, ZnS concentration has an important role in formation of heterojunctions between TiO_2/ZnS nanocomposites. It results in inhibition of electron/hole pair recombination.[56,57] Average pore size distribution was calculated using the Barrett–Joyner–Halenda (BJH) method and the values were 9.79, 9.31, 8.98, 8.88 and 6.82 nm for Ti, TiZ-1, TiZ-2, TiZ-3 and TiZ-4, respectively. Such pore size analysis revealed that higher concentration of ZnS reduces the pore size of mesoporous spheres by occupying pores of the network. This significantly suppresses the interaction of organic pollutants with the photocatalyst.

To elucidate the photocatalytic process under visible light, active species generated during the reaction were identified by free radical and hole scavenging experiments. Hydroxyl radicals ($^{\cdot}OH$), holes (h^+) and superoxide anions ($O_2^{-}\cdot$) are possible active species in photodegradation of organic pollutants.[37,44] To detect the active species during the photocatalytic reaction, benzoic acid (BA), the sodium salt of ethylenediamine tetraacetate (EDTA) and potassium persulphate ($K_2S_2O_8$) were introduced into the catalyst solution as scavengers, respectively, of hydroxyl radicals, holes and superoxide radical anion.[41,47] Fig. 13(a) presents the photodegradation of MB catalysed by TiO_2/ZnS (TiZ-1) in the presence of these various scavengers under visible light illumination. Compared with the scavenger-free system, the dye degradation efficiency in the presence of $O_2^{-}\cdot$ scavenger was 91.93%. In contrast, the reaction with the addition of h^+ scavenger EDTA, was almost inhibited with 38% of MB degradation after 32 min. To further determine the degradation mechanism, another experiment was performed using the BA scavenger. The photocatalytic activity was greatly reduced in the presence of the $O_2^{-}\cdot$ scavengers, with 54% MB degraded in 32 min. These results strongly suggest that hydroxyl radicals, holes and superoxide radical anions all contribute to photodegradation, but that the hole is a key intermediate as trapping – it totally inhibited photodegradation. It can be concluded that hole (h^+) radical is the major oxidative species responsible for photooxidative conversion of MB.[58]

The stability of a photocatalyst is important for practical applications, thus the TiO_2/ZnS composite photocatalyst was recycled under the same conditions. Fig. 13(b) shows the reusability of TiZ-1 photocatalyst for degradation of MB examined over three cycles of 32 min under visible light irradiation. After the photocatalysis experiments, the catalyst was separated from the reaction mixture by centrifugation and the concentration of the dye solution was adjusted to its initial value. Photocatalysts were reused for three cycles and the obtained degradation values were 90.90, 90.64 and 89.92% for the first, second and third cycles, respectively. The photocatalytic efficiency of the TiO_2/ZnS composites did not decline significantly, suggesting that the catalyst has good stability and sustainability. Fig. S2† shows the XRD patterns of the TiO_2/ZnS composites before and after four runs of photocatalytic activity under the visible light irradiation for degradation of MB. It can be clearly observed that the phase and structure of the TiO_2/ZnS composite were unchanged after the photocatalytic cycles; suggesting that the sample was stable under the present photocatalytic degradation process. In addition, the photocatalytic structural stabilities and photocatalytic loss of TiO_2/ZnS composites were investigated using XPS spectra, as shown in Fig. S2.† The binding energies of Zn 2p, Ti 2p, O 1s and S 2p of the recycled TiO_2/ZnS showed no peak-shift compared with those of the fresh sample, inferring that the chemical states of Zn, Ti, O and S elements in TiO_2/ZnS did not change during the reaction process.
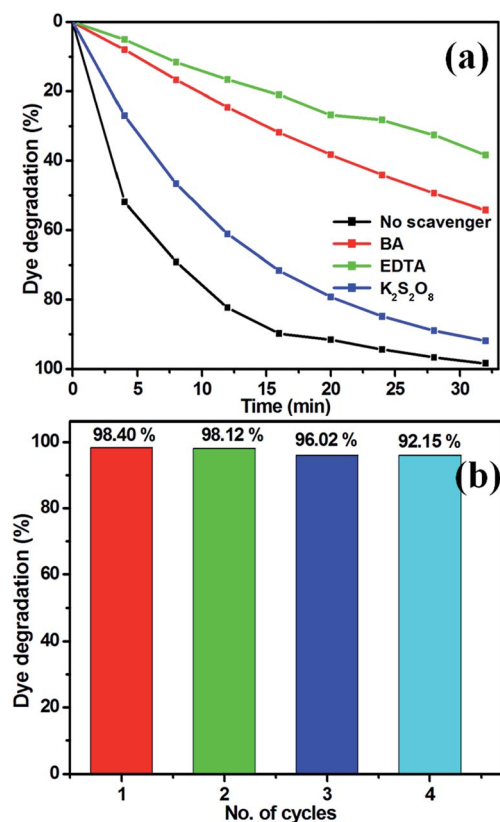

Fig. 13 (a) Effect of MB degradation over TiO_2/ZnS in the presence of various scavengers and (b) reusability of sample TiZ-1 under visible light irradiation.

Kinetic study

The rate of photocatalytic reduction of the nanocomposites can be described by pseudo-first-order kinetics, so plots of $\ln(C_0/C_t)$ *versus* irradiation time for the adsorption and degradation of MB on TiO_2/ZnS nanocomposites were examined. The $\ln(C_0/C_t)$ curves *versus* irradiation time were linear, indicative of good correlation to first-order kinetics (Fig. 14(a)). The apparent rate constant K was calculated to be 0.0428, 0.1199, 0.0675, 0.0591 and 0.0526 min^{-1} for Ti, TiZ-1, TiZ-2, TiZ-3 and TiZ-4, respectively. K value decreased with addition of ZnS at concentrations from 0.025 M to 0.1 M (0.1199 min^{-1} to 0.0526 min^{-1}). The K for the TiO_2/ZnS sample was 0.1199 min^{-1}, 2.5 times higher than that of pure TiO_2 (0.0428 min^{-1}). The kinetic data obtained using the pseudo-first order model such as apparent rate constants (K_{app}), corresponding correlation coefficients (R^2) and maximum dye degradation in the presence of TiO_2/ZnS
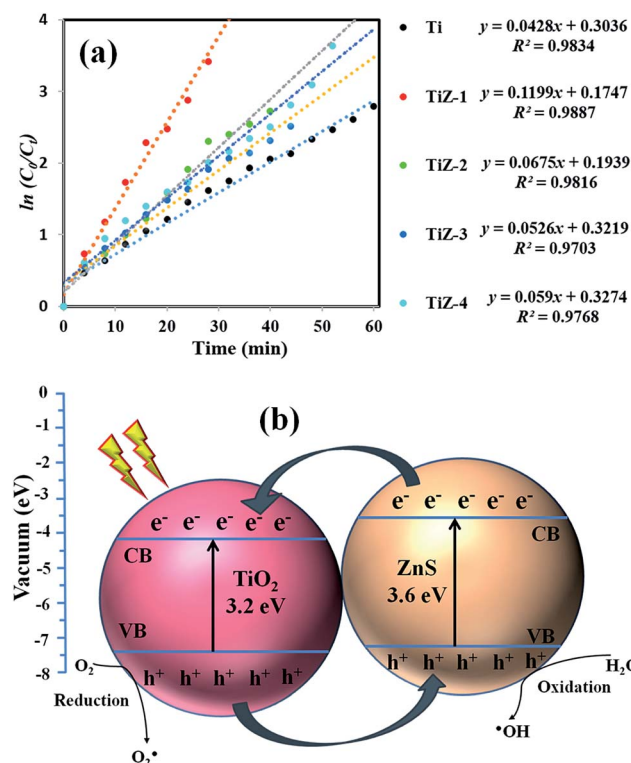
Fig. 14 (a) Plots of $\ln(C_0/C_t)$ as a function of time (min) for the photodegradation of MB over the TiO_2/ZnS nanocomposites, and (b) photocatalytic mechanism of TiO_2/ZnS nanocomposites.

nanostructures are presented in Table 1. Introduction of ZnS quantum dots into the mesoporous TiO_2 was in favour of high increased photocatalytic activity and suppressed the recombination of photogenerated electron/hole pairs.[59,60]

Schematic representation of photocatalytic activity of mesoporous TiO_2/ZnS nanocomposites is shown in Fig. 14(b). When the light is irradiated, the visible light provides the photons required to generate electron and hole pairs. The conduction band (CB) of TiO_2 lies at a more positive potential than that of ZnS, while the valence band (VB) of ZnS is more negative than that of TiO_2. From the energy band diagram, it was found that an electron from the bottom of the CB of ZnS quickly transferred to the CB of TiO_2. Meanwhile, the photogenerated hole transfer could take place from the VB of TiO_2 to the VB of ZnS,

suggesting that the photogenerated electrons and holes were efficiently separated.[61] Such band structure facilitates separation of the excited electrons and hole pairs, and facilitates redox reactions where electrons reduce dissolved molecular oxygen to produce superoxide radical anions ($^{\bullet}O_2^-$), while holes oxidize H_2O molecular to yield hydroxyl radicals ($HO^{\bullet}$) on the TiO_2/ZnS surfaces. Organic dye pollutants (MB) are eventually oxidized by these highly active species to CO_2 and H_2O products.[62]

Conclusion

Assessment of photocatalytic degradation of organic compounds using the TiO_2/ZnS mesoporous nanostructures revealed a remarkably higher reaction rate under visible light irradiation compared with that of pure mesoporous TiO_2. Impregnation of ZnS quantum dots was confirmed by XPS and elemental analysis. The investigation of photocatalytic activity indicated that the TiO_2/ZnS nanocomposites possessed higher photocatalytic activity compared with mesoporous TiO_2 for degradation of MB under visible light irradiation. The maximum degradation efficiency was observed for 0.025 M of ZnS, where the MB related absorption peak completely disappeared after 32 min of irradiation. Photogenerated holes (h^+) over TiO_2/ZnS supported photocatalysts in the photodegradation of organic pollutants. After four cycles of reuse, the catalyst showed significant capacity for dye degradation.

Acknowledgements

References

1 X. Yu, Z. Zhao, J. Zhang, W. Guo, L. Li, H. Liu and Z. L. Wang, *CrystEngComm*, 2017, **19**, 129–136.

2 S. Harish, J. Archana, M. Sabarinathan, M. Navaneethan, K. D. Nisha, S. Ponnusamy, C. Muthamizhchelvan, M. Shimomura, H. Ikeda, D. K. Aswal and Y. Hayakawa, *Appl. Surf. Sci.*, 2016, DOI: 10.1016/j.apsusc.2016.12.082.

3 S. Vadivel, D. Maruthamani, A. Habibi-Yangjeh, B. Paul, S. S. Dhar and K. Selvam, *J. Colloid Interface Sci.*, 2016, **480**, 126–136.

4 S. Harish, M. Navaneethan, J. Archana, A. Silambarasan, S. Ponnusamy, C. Muthamizhchelvan and Y. Hayakawa, *Dalton Trans.*, 2015, **44**, 10490–10498.

5 X. Lang, W. Ma, C. Chen, H. Ji and J. Zhao, *Acc. Chem. Res.*, 2014, **47**, 355–363.

6 K. Sunada, X. G. Ding, M. S. Utami, Y. Kawashima, Y. Miyama and K. Hashimoto, *J. Agric. Food Chem.*, 2008, **56**, 4819–4824.

7 Y. Lu, H. Yu, S. Chen, X. Quan and H. Zhao, *Environ. Sci. Technol.*, 2012, **46**, 1724–1730.

Table 1 Observed pseudo-first-order rate constants, R^2 values, maximum degradation (%) and time required for maximum degradation of TiO_2/ZnS nanocomposites

Sample	K_{app} (TiO_2/ZnS)	R^2	Maximum degradation (%)	Time taken for maximum degradation (min)
Ti	0.0428	0.9834	84.27	60
TiZ-1	0.1199	0.9887	98.40	32
TiZ-2	0.0675	0.9816	93.42	40
TiZ-3	0.0590	0.9768	91.89	44
TiZ-4	0.0526	0.9703	97.36	52

8 R. Richter, T. Ming, P. Davies, W. Liu and S. Caillol, *Prog. Energy Combust. Sci.*, 2017, **60**, 68–96.

9 J. Archana, M. Navaneethan and Y. Hayakawa, *J. Power Sources*, 2013, **242**, 803–810.

10 J. Archana, S. Harish, M. Sabarinathan, M. Navaneethan, S. Ponnusamy, C. Muthamizhchelvan, M. Shimomura, H. Ikeda, D. K. Aswal and Y. Hayakawa, *RSC Adv.*, 2016, **6**, 68092–68099.

11 S. Chen, H. Wang, L. Zhu, J. Li and J. Sun, *Appl. Surf. Sci.*, 2014, **321**, 86–93.

12 Z. Lianjie, L. Kun, L. Hongbin, S. Youguang and Q. Mo, *Solid State Sci.*, 2013, **20**, 8–14.

13 L. Wei, W. Zhangxiong, W. Jinxiu, A. A. Elzatahry and Z. Dongyuan, *Chem. Mater.*, 2014, **26**, 287–298.

14 R. O. Da Silva, R. H. Galves, D. G. Stroppa, A. J. Ramirez and E. R. Leite, *Nanoscale*, 2011, **3**, 1910–1916.

15 X. Liu, Y. Gao, C. Cao and H. Luo, *Langmuir*, 2010, **26**, 7671–7674.

16 A. Fujishima, T. N. Rao and D. A. Tryk, *J. Photochem. Photobiol., C*, 2000, **1**, 1–21.

17 A. Fujishima, X. Zhang and D. A. Tryk, *Int. J. Hydrogen Energy*, 2007, **32**, 2664–2672.

18 M. Yan, L. Yuanzhi, M. Mingyang, H. Jingtao, Z. Min and Z. Xiujian, *J. Mater. Chem. A*, 2015, **3**, 5509–5516.

19 G. Weiyin, W. Minqiang, R. Chenxin, Y. Xi, Y. Honghui, L. Jing, H. Delong and B. Jinbo, *Nanoscale*, 2014, **6**, 5498–5508.

20 S. Harish, M. Sabarinathan, J. Archana, M. Navaneethan, K. D. Nisha, S. Ponnusamy, V. Gupta, C. Muthamizhchelvan, D. K. Aswal, H. Ikeda and Y. Hayakawa, *Appl. Surf. Sci.*, 2016, DOI: 10.1016/j.apsusc.2017.01.164.

21 H. Choonyian, C. Weesiong, S. A. Rahman, P. Khiew, S. Radiman, R. A. Shukor, M. A. A. Hamid and N. Ghazali, *New J. Chem.*, 2016, **40**, 1124–1136.

22 H. Luyang, Z. Yumin, Z. Shanmei and L. Benxia, *RSC Adv.*, 2016, **6**, 43098–43103.

23 M. Zalfani, B. Schueren, H. Zhi-Yi Hu, J. C. Rooke, R. Bourguiga, M. Wu, Y. Li, G. V. Tendeloo and S. Bao-Lian, *J. Mater. Chem. A*, 2015, **3**, 21244–21256.

24 F. Xin, Z. Wendong, S. Yanjuan, H. Hongwei and D. Fan, *Environ. Sci.: Nano*, 2017, **4**, 604–612.

25 C. Mondal, M. Ganguly, J. Pal, A. Roy, J. Jana and T. Pal, *Langmuir*, 2014, **30**, 4157–4164.

26 F. Xin, Z. Wendong, D. Hua, N. Zilin, D. Fan and Z. Yuxin, *J. Hazard. Mater.*, 2017, **322**, 223–232.

27 Y. Kim, S. J. Kim, C. Sung-Pyo, B. H. Hong and J. Du-Jeon, *Sci. Rep.*, 2015, **5**, 12345–12353.

28 C. Wang, Y. Ao, P. Wang, J. Hou, J. Qian and S. Zhang, *Mater. Lett.*, 2010, **64**, 439–441.

29 Y. Guo, L. Wang, L. Yang, J. Zhang, L. Jiang and X. Ma, *Mater. Lett.*, 2011, **65**, 486–489.

30 Y. C. Zhang, Z. N. Du, S. Y. Li and M. Zhang, *Appl. Catal., B*, 2010, **95**, 153–159.

31 S. Vaclav, B. Snejana, M. Nataliya, H. Vendula and L. Kamil, *Microporous Mesoporous Mater.*, 2008, **110**, 370–378.

32 Y. Xiaodan, W. Qingyin, J. Shicheng and G. Yihang, *Mater. Charact.*, 2006, **57**, 333–341.

33 S. Srinivasa Rao, D. Punnoose, C. V. Tulasivarma, C. H. S. S. Pavan Kumar, C. V. V. M. Gopi, S. K. Kim and H. J. Kim, *Dalton Trans.*, 2015, **44**, 2447–2455.

34 A. Franco, M. C. Nevew, M. M. L. Ribeiro Carrott, M. H. Mendonca, M. I. Pereira and O. C. Monteiro, *J. Hazard. Mater.*, 2009, **161**, 545–550.

35 X. Chen, F. Zhang, Q. Wang, X. Han, X. Li, J. Liu, H. Lin and F. Qu, *Dalton Trans.*, 2015, **44**, 3034–3042.

36 C. Mondal, A. Singh, R. Sahoo, A. K. Sasmal, Y. Negishi and T. Pal, *New J. Chem.*, 2015, **39**, 5628–5635.

37 M. Sabarinathan, S. Harish, J. Archana, M. Navaneethan, H. Ikeda and Y. Hayakawa, *RSC Adv.*, 2016, **6**, 109495–109505.

38 T. Ohsaka, *J. Phys. Soc. Jpn.*, 1980, **48**, 1661–1668.

39 B. Karunagaran, K. Kim, D. Mangalraj, J. Yi and S. Velumani, *Sol. Energy Mater. Sol. Cells*, 2005, **88**, 199–208.

40 Y. Li, Y. Duan and W. Li, *Spectrosc. Spectral Anal.*, 2000, **20**, 699–701.

41 L. Kong, Z. Li, S. Huang, J. Jia and L. Li, *Appl. Catal., B*, 2017, **204**, 403–410.

42 H. Yu, W. Chen, X. Wang, Y. Xu and J. Yu, *Appl. Catal., B*, 2016, **187**, 163–170.

43 R. Sanjines, H. Tang, H. Berger, F. Gozzo, G. Margaritondo and F. Levy, *J. Appl. Phys.*, 1994, **75**, 2945–2951.

44 Z. Jingxin, Z. Shule, C. Wei and Q. Zhong, *Appl. Surf. Sci.*, 2013, **268**, 535–540.

45 C. V. Reddy, J. Shima and M. Cho, *J. Phys. Chem. Solids*, 2017, **103**, 209–217.

46 S. Ameen, M. Shaheer and H. S. Shin, *J. Chem.*, 2013, **29**, 837–860.

47 Z. Ali, S. N. Cha, J. I. Sohn, I. Shakir, C. Yan, J. M. Kim and D. J. Kang, *J. Mater. Chem.*, 2012, **22**, 17625–17629.

48 Y. Zhao, C. Li, X. Liu, F. Gu, H. L. Du and L. Shi, *Appl. Catal., B*, 2008, **79**, 208–215.

49 L. V. Garciaa, M. I. Mendivila, G. Garcia Guillena, J. A. Aguilar Martineza, B. Krishnana, D. Avellanedaa, G. A. Castilloa, T. K. Das Roya and S. Shajia, *Appl. Surf. Sci.*, 2015, **336**, 329–334.

50 D. A. Zatsepin, D. W. Boukhvalov, N. V. Gavrilov, A. F. Zatsepin, V. Y. Shur, A. A. Esin, S. S. Kim and E. Z. Kurmaev, *Appl. Surf. Sci.*, 2017, **400**, 110–117.

51 NIST XPS Database (Web-version), rev. 4.1, http://srdata.nist.gov/xps/, called 2016-07-21.

52 C. He, Y. Yu, X. Hu and A. Larbot, *Appl. Surf. Sci.*, 2002, **200**, 239–247.

53 Y. L. Lin, T. J. Wang and Y. Jin, *Powder Technol.*, 2002, **123**, 194–198.

54 L. Zheng, Y. Zheng, C. Chen, Y. Zhan, X. Lin, Q. Zheng, K. Wei and J. Zhu, *Inorg. Chem.*, 2009, **48**, 1819–1825.

55 M. R. Hoffmann, S. T. Martin, W. Choi and D. W. Bahnemann, *Chem. Rev.*, 1995, **95**, 69–72.

56 A. A. Ismail and D. W. Bahnemann, *J. Mater. Chem.*, 2011, **21**, 11686–11707.

57 M. Faisal, A. A. Ibrahim, F. A. Harraz, H. Bouzid, M. S. Al-Assiri and A. A. Ismail, *J. Mol. Catal. A: Chem.*, 2015, **397**, 19–25.

58 Y. Xia, Q. Li, K. Lv and M. Li, *Appl. Surf. Sci.*, 2017, **398**, 81–88.

59 H. Jia, W. He, W. G. Wamer, X. Han, B. Zhang, S. Zhang, Z. Zheng, Y. Xiang and Y. Jun-Jie, *J. Phys. Chem. C*, 2014, **118**, 21447–21456.

60 M. Vautier, C. Guillard and J. M. Herrmann, *J. Catal.*, 2001, **201**, 46–59.

61 Q. Xiaofei, H. Yuchen, W. Chengpeng, D. Fanglin and C. Lixin, *RSC Adv.*, 2015, **5**, 5307–5311.

62 Z. Yunlong, Z. Haijiao, C. Longli, M. Yu, H. Le, D. Guoji, J. Zheng, B. Lifeng, N. Manhtai and Z. Guanghong, *Eur. J. Inorg. Chem.*, 2015, 2895–2900.